Available online at www.sciencedirect.com

ScienceDirect

journal homepage: www.elsevier.com/locate/he

Remarkable visible-light induced hydrogen generation with $ZnIn_2S_4$ microspheres/$CuInS_2$ quantum dots photocatalytic system

Onur Cavdar [a], *Anna Malankowska* [a], *Daniel Amgar* [b], *Paweł Mazierski* [a], *Justyna Łuczak* [c], *Wojciech Lisowski* [d], *Adriana Zaleska-Medynska* [a,*]

[a] *Department of Environmental Technology, Faculty of Chemistry, University of Gdansk, Gdansk, 80-308, Poland*
[b] *Department of Physics of Complex Systems, Faculty of Physics, Weizmann Institute of Science, Rehovot, 761000, Israel*
[c] *Department of Process Engineering and Chemical Technology, Faculty of Chemistry, Gdansk University of Technology, Gdansk, 80-233, Poland*
[d] *Institute of Physical Chemistry, Polish Academy of Sciences, Warsaw, 01-224, Poland*

HIGHLIGHTS

- $ZnIn_2S_4$ microspheres/$CuInS_2$ quantum dots photocatalytic system was synthesized.
- Photocatalytic system loaded ny Pt NPs are able to generate H_2 under visible light.
- Visible light activity range reaches up to a wavelength of 540 nm.
- Light harvesting property of the system was enhanced by $CuInS_2$ quantum dots.

GRAPHICAL ABSTRACT

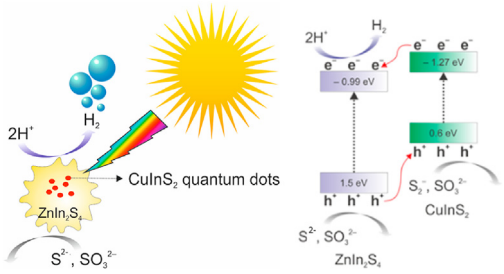

ARTICLE INFO

Article history:
Received 27 July 2020
Received in revised form
17 September 2020
Accepted 24 September 2020
Available online 21 October 2020

ABSTRACT

A new and active material in the form of $ZnIn_2S_4$ microspheres decorated by $CuInS_2$ quantum dots have been obtained by hydrothermal method for the first time. The optimum amount of $CuInS_2$ quantum dots (1.13 wt.%) introduced into rection medium during $ZnIn_2S_4$ microspheres synthesis increased the photocatalytic H_2 generation rate by 2.5 times than that of bare $ZnIn_2S_4$ photocatalysis under visible light irradiation. This sample exhibited strong photoactivity in the extended visible range up to 540 nm with 30.6% apparent quantum efficiency ($\lambda = 420$ nm).

* *Corresponding author.*
E-mail addresses: adriana.zaleska@ug.edu.pl, adriana.zaleska-medynska@ug.edu.pl (A. Zaleska-Medynska).

https://doi.org/10.1016/j.ijhydene.2020.09.212

Introduction

As many efforts have being devoted to find the most promising green energy source, H_2 is one of the most conspicuous fuel due to its high specific energy value (33 kWh/kg) and clean by-products relatively to conventional fossil fuels [1,2]. However, the current H_2 market relies on mostly steam reforming of natural gas which requires high energy input and releases greenhouse gas emission while another well-known method, electrolysis requires an external circuit to split water to O_2 and H_2 fuel [3]. After the work by Fujishima and Honda [4], photogenerated H_2 evolution (PHE) by splitting water using TiO_2 semiconductor photocatalysis *via* irradiation of semiconductors by a light source has been ranked as another green way to generate H_2 fuel. Beyond TiO_2, many other semiconductors have been studied also such as ZnS [5], ZnO [6], $SrTiO_3$ [7], Co_3O_4 [8], $LaFeO_3$ [9], $Ba_5Ta_4O_{15}$ [10], $BaZrO_3$ [11] and $CaTiO_3$ [12]. Nevertheless, one of the limitations of those materials is wide bandgap which make them active only under UV light that comprise 4% of solar spectrum on the earth surface [13]. Therefore, seeking for new materials which are active under visible light spectrum is crucial to produce H_2 fuel by PHE in terms of green technology.

One of the types of AB_2X_4 family, $ZnIn_2S_4$, is considered a promising candidate for PHE under visible light due its suitable band gap (2.3 eV) and stability [14]. Several synthesis method have been proposed that allowed to obtain various shapes of that semiconductor photocatalyst such as microspheres, nanotubes, nanoribbons, monolayers [15,16]. In order increase performance of $ZnIn_2S_4$ under visible light, it is pivotal to inhibit the photo-generated hole and electron recombination that leads to better charge separation on $ZnIn_2S_4$ surface or narrow the band gap of $ZnIn_2S_4$. Various methods have been studied to achieve these goals. For instance, visible light induced $ZnIn_2S_4$ has been reached by Cu doping [17] whereas combination with different carbon-based analogs [18] or formation of heterostructures using other semiconductors $BiVO_4$ [19], $MoSe_2$ [20], g-C_3N_4 [21], WO_3 [22] have been investigated for better charge separation on $ZnIn_2S_4$ or boosting photogenerated electron transfer to the catalytically active sites of heterostructures which is required for better PHE performance. Another alternative for the formation of heterostructures, using quantum dots have also been studied to decorate larger semiconductor matrix materials and this approach has been widely studied for ZnO [23,24], TiO_2 [25,26] and g-C_3N_4 [27,28]. Quantum dots are basically type of material that exhibits unique properties which arises with particle size lower than the bulk-exciton Bohr radius due to changes in the surface-to-volume ratio and quantum confinement effect [29,30]. Generally saying, a presence of quantum dots on a larger semiconductor matrix induces the activity more than of larger size of nanoparticles due to the relatively higher surface to volume ratio of quantum dots that creates more active site for PHE and high capability of light-harvesting [31]. Among them, CdS [32], MoS_2 [15,33] and carbon [13,18] dots have been used to decorate $ZnIn_2S_4$. Recently, $CuInS_2$ quantum dots have drawn attention as its suitability for visible light-driven PHE applications [34]. Although there are several reports on PHE such as $CuInS_2$/ZnS quantum dots [35,36] and $CuInS_2$ quantum dots hybridized polymeric carbon nitride, nevertheless, there is no report on $CuInS_2$ quantum dots decorated $ZnIn_2S_4$ semiconductor for PHE application. To the best of our knowledge, only studies regarding $ZnIn_2S_4$/$CuInS_2$ system have been reported by Guan et al. and Guo et al. which have been based on 2D-2D structure [37] and core-shell structure [38], respectively.

Herein, $ZnIn_2S_4$ microspheres (ZIS) in the presence of different amount of $CuInS_2$ quantum dots (CIS) were synthesized to obtain CIS decorated ZIS heterostructures (ZIS/CIS) for PHE under visible light irradiation using simple hydrothermal method for the first time. Fixed amount of Pt metal co-catalyst was deposited on the obtained ZIS/CIS samples with different CIS amounts using photodeposition method for photocatalytic hydrogen evolution experiments under visible light irradiation. We find that optimum amount pre-prepared CIS introduced to ZIS hydrothermal reaction medium enhance the photocatalytic hydrogen generation activity of ZIS.

Experimental

Materials

Cetyltrimethylamonium bromide (CTAB, 95%) (Aldrich), indium (III) nitrate hydrate (99.99%) (Alfa Aesar), thioacetamide (J.T. Baker, Avantar performance materials), copper (I) iodide (99.99%) and indium (III) acetate (99.99%) (Acros Organics), zinc sulfate heptahydrate (CHEMPUR), chloroplatinic acid hexahydrate (Sigma-Aldrich). All chemicals were used without any further purification.

Synthesis of $CuInS_2$ quantum dots

$CuInS_2$ quantum dots (CIS) synthesis method has been adopted from Booth [39]. The solid mixture of indium acetate, copper iodide, thiourea and mercaptoundecanoic acid (MUA) with 1:1:2:4 M ratio was added into a 50 ml 3-necked round bottom flask. The flask was connected to the basic reflux system with tap water cooling and placed into an oil bath and the temperature was controlled by the immersing thermocouple into the oil bath (the temperature of the oil bath was about 10 °C higher than the reaction mixture). The solid mixture was mixed gently by a magnetic stirrer bar and temperature of the oil bath was increased to 120 °C slowly. Meanwhile, a yellow-red opaque thick liquid has been observed between 90 and 100 °C (Fig. S1b). Then, the blocker on the light neck was replaced with glass nozzle to purge the reaction mixture with nitrogen gas for 30 min while the temperature of the oil bath was slowly increased to 150 °C. After that, the blocker was reset and the oil bath temperature was heated to 190 °C and the color changing was observed that followed in order of yellow/red and dark red (Fig. S1b, c, d) as indicated by Booth. As reaching the dark red product, the flask was immediately placed into an ice bath. Following the temperature drop, approximately 40 ml of isopropanol have been added into the flask with as formed CIS and the flask were sonicated for 15 min. Finally, the CIS-isopropanol mixture was centrifuged and washed with isopropanol several times and dried at 60 °C under atmospheric pressure for 12 h. The

product was grinded using an agate mortar and the obtained red powder was kept in a cool and dry place in a glass container.

Solubility test for $CuInS_2$ quantum dots under alkaline conditions

Due to the poor solubility of MUA capped CIS in water (pH 7) and in ZIS microspheres precursor environment (pH 2), the solubility and PL property of MUA capped CIS quantum dots was also tested in an alkaline solution with different pH levels whether their solubility is higher in alkaline conditions. For that purpose, 20 ml water-CIS quantum dots mixture (1 mg/ml) was prepared (pH = 7). The mixture was mixed for 30 min using magnetic stirrer. As expected, CIS aggregated and could not be dissolved in the water. Later, 25% ammonia water was added dropwise to adjust pH. At each pH level, a sample was collected with a Pasteur pipette and PL intensity was measured swiftly (excitation wavelength: 330 nm). The pH level was controlled using both pH meter and pH-indicator paper.

Synthesis of $CuInS_2$ quantum dots decorated $ZnIn_2S_4$ microspheres

CIS decorated $ZnIn_2S_4$ microspheres (ZIS) were synthesized using hydrothermal method. ZIS preparation was adopted from Shen et al. [17]. 6.1 mmol (1.75 g) $ZnSO_4{\cdot}7H_2O$, 12.08 mmol (3.85 g) $In(NO_3)_3{\cdot}H_2O$, 4.25 mmol (1.55 g) cetrimonium bromide and 41.26 mmol (3.10 g) thioacetamide were added to 120 ml deionized water (Mixture A) in a glass beaker and mixed with a magnetic stirrer bar. The mixture A was left for stirring while pre-prepared CIS–water mixture (Mixture B) were prepared by adding 50, 100, 150 or 200 mg CIS to 10 ml water in a beaker and sonicated for 30 min. Later, the mixture B was added to mixture A and remaining CIS in the beaker were rinsed 10 ml of water and transferred to mixture A. The final mixture (140 ml) was stirred for 10 min vigorously and finally transferred quickly to Teflon-lined stainless-steel autoclave reactor with 200 ml volume for the hydrothermal reaction. The weight ratios of CIS to ZIS precursors plus CIS in the hydrothermal reaction were 0.57 wt%, 1.13 wt%, 1.69 wt% and 2.24 wt% CIS for 50, 100, 150 or 200 mg CIS addition and products were abbreviated as ZIS/CIS_50, ZIS/CIS_100, ZIS/CIS_150 and ZIS/CIS_200, respectively The reaction was carried out at 160 °C for 12 h and the reactor was cooled under room temperature. The obtained product was washed with excess amount of ethanol and centrifuged several times for 10 min at 6000 rpm. Later, the product was dried at 60 °C under atmospheric pressure. ZIS without CIS decoration was synthesized by the as mentioned method above, except without any CIS in the hydrothermal reaction medium. Finally, the Pt deposition (0.75 wt%) on ZIS and ZIS/CIS samples were carried out using photodeposition technique.

Photodeposition of Pt

Pt was selected as a cocatalyst for ZIS and ZIS/CIS photocatalysts. To obtain Pt deposited ZIS/CIS, photodeposition technique was used. 500 mg ZIS or ZIS/CIS was mixed with 17.5 ml ethanol in a glass beaker and ultrasonicated for 10 min. The mixture was transferred to quartz glass photoreactor with 25 ml volume. Then, $H_2PtCl_6{\cdot}6H_2O$ aqueous solution was added to ethanol-photocatalyst (0.75 wt % of Pt) mixture. The final mixture was mixed in the dark for 2 h and the headspace of the reactor degasified with nitrogen for 1 h. Finally, the reactor was irradiated using Xenon lamp (Oriel, 66,021, 1000 W) at 25 °C for 1 h. The dark yellow product was washed with excess amount of ethanol and centrifuged at 6000 rpm. Later, the product was dried at 60 °C under atmospheric pressure.

Characterization

The particle size, shape, and morphology of samples have been analyzed by high-resolution transmission electron microscopy images and EDS maps were recorded in a double aberration-corrected Themis Z microscope (Thermo Fisher Scientific Electron Microscopy Solutions, Hillsboro, USA) equipped with a high-brightness FEG at an accelerating voltage of 200 kV. HAADF scanning TEM images were recorded with a Fishione Model 3000 detector (E.A. Fischione Instruments Inc., Export, PA, USA) with a semi-convergence angle of 30 mrad, a probe current of 50 pA and scanning electron microscopy (JEOL JSM-7001F and JEOL JSM-7610F operating at 15 kV). Transmission electron microscopy (TEM) was performed using bright-field (BF) to analyze ZIS/CIS_100 and ZIS/CIS_100-Pt samples with a Hitachi H-800 microscope (Hitachi High-Technologies), operating at 150 kV. The TEM samples were prepared by dry transfer of powder to carbon on copper grid (Agar Scientific), and imaged with dose rate not exceeding 20,000 $e^-/nm^2/s$. Dose rate above 40,000 $e^-/nm^2/s$ led to the remodeling of the substrate and the coagulation of Pt species into larger nanocomplexes. X-ray diffractometer (XRD, Rigaku MiniFlex 600) equipped with Cu Kα irradiation in the 2θ range of 20–80° was used to identify the crystalline structure. The Pt and Cu content were analyzed by inductively coupled plasma optical emission spectroscopy (ICP-OES) using Agilent 5100 spectrometer, according to PN-EN ISO 11885:2009 standard. The mineralization was performed before the samples' analysis. The high-resolution (HR) XPS spectra were recorded by a PHI 5000 VersaProbe - Scanning ESCA Microprobe (ULVAC-PHI, Japan/USA) using monochromatic Al-Kα radiation (hν = 1486.6 eV) with the energy step size of 0.1 eV at the pass energy of 23.5 eV and the X-ray source operating under the following conditions: 15 kV, 25 W, 100 μm spot. The analyzed area was 250 μm × 250 μm. The binding energy (BE) scale was referenced to the C 1s peak with BE = 284.8 eV. The UV–vis spectra of samples were recorded in the scan range 200–800 nm using UV–vis spectrophotometer (Evolution 220, Thermo Scientific) equipped with an integrating sphere and $BaSO_4$ as the reference (Labsphere certified reflectance standard). The photoluminescence spectra (PL) were recorded using a PerkinElmer Luminescence Spectrometer LS-50B equipped with Xenon discharge lamp as an excitation source. The samples were excited with 330 nm at room temperature and the emission was scanned between 300 and 800 nm. Fourier-transform infrared spectroscopy (FTIR) (Bruker, IFS66) was used to identify the surface characteristics of CIS in the scan range of 500–5000 cm^{-1} in the diffuse reflectance mode with a resolution of 0.12 cm^{-1} at room

temperature. KBr was used as a reference material. Surface area and pore volume were analyzed by Gemini V200 Surface Area Analyzer (Micrometrics) equipped in degassing unit. The apparatus was checked with Carbon Black reference material with specific surface area of 30.6 m^2/g.

Photogenerated hydrogen evolution and stability

The photocatalytic hydrogen evolution performance (PHE) test of obtained ZIS/CIS–Pt photocatalysts were carried out using the procedure as follows. 100 mg photocatalyst powder was mixed with 80 ml of 0.35 M Na_2S/0.25 M Na_2SO_3 aqueous solution of sacrificial agent. The mixture was ultrasonicated for 10 min and transferred to a quartz glass photoreactor (V = 110 ml) with a cooling jacket. The mixture was then irradiated using a 1000 W Xenon lamp (Oriel, 66,021) which emitted both UV and visible irradiation. UV light was removed by a cut-off filter GG420 (λ > 420 nm). The temperature of the reactor was kept at 10 °C by a thermostat. Before PHE, the headspace of the reactor was purged with nitrogen gas with 10–12 dm^3/h velocity for 30 min under dark while the mixture was mixed with a magnetic stirrer bar. 200 μl of gas sample were collected within every hour from the headspace of the photoreactor using an air-tight syringe (Hamilton) and injected to the gas chromatograph (Thermo Scientific TRACE 1300-GC), coupled with thermal conductivity detector (TCD). No hydrogen generated by the irradiation of sacrificial agent solution with the same conditions. Photostability cycle runs were conducted under same conditions but using cut-off filter GG455 (λ > 455 nm). The calibration experiments for the calculations to detect amount hydrogen evolution was followed by introducing different volume of pure hydrogen gas to the quartz glass photoreactor with the same conditions as mentioned above and plus a digital manometer was connected to the reactor to monitor the pressure change in the headspace of the photoreactor. Ideal gas equation has been used to calculate the amount of hydrogen in moles.

Action spectra analysis for photocatalytic hydrogen evolution reaction

Action spectra analysis was performed in the presence of sample with the highest hydrogen evolution rate, namely ZIS/CIS_100-Pt, using the procedure as follows. 12.5 mg ZIS/CIS_100-Pt sample was mixed with 10 ml of 0.35 M Na_2S/0.25 M Na_2SO_3 aqueous solution of sacrificial agent and ultrasonicated for 5 min and transferred to a Teflon photoreactor (V = 15 ml) with a quartz window and cooling jacket. The photoreactor was connected to a measuring system consisting of a tunable monochromatic light sources (1000 W Xe lamp – LSH602 and monochromator – MSW306, LOT-Quantum Design), GC-BID (BID-2010 Plus, Shimadzu) and FTIR (not used in this study). Then, the headspace of the photoreactor was purged with helium gas for 30 min under dark while the suspension was mixed with a magnetic stirrer bar. The temperature of the reactor was kept at ambient temperature. The sample was irradiated with the following wavelengths: 420, 440, 460, 480, 500, 540 and 600 nm. Irradiation intensity (W) was measured for individual wavelengths with optical meter (ILT2400, International Light technologies). No hydrogen generated by the irradiation of sacrificial agent solution with the same conditions. The calibration experiments for the calculations to detect amount hydrogen evolution was followed by introducing different volume of pure hydrogen gas to the quartz glass photoreactor with the same conditions as mentioned above and plus a digital manometer was connected to the reactor to monitor the pressure change in the headspace of the photoreactor. Ideal gas equation has been used to calculate the amount of hydrogen in moles.

The apparent quantum efficiency as a function of wavelength was calculated based on the ratio of rate of hydrogen generation to the flux of incident photons, assuming that two photons are required according to the reaction stoichiometry, starting calculations from Eq. (1).

$$AQE(\%) = \frac{2 \times \text{number of evolved } H_2 \text{ molecules}}{\text{number of incident photos}} \quad (1)$$

Results and discussion

The characteristics of CIS were investigated by their particle shape, size distribution, PL emission and FTIR spectra HAADF-STEM image of CIS (Fig. S2a) revealed that the size range of dots ranged between 1.8 and 2.4 nm. Two peaks around 420 and 660 nm can be seen from PL spectra of CIS. The first broad peak located around 420 nm can be attributed to nonradiative transition of excited electrons on conduction band bottom to sub-bands due to the surface defects or sulfur vacancies on CIS whereas the second red shifted peak (660 nm) can be based on the radiative transition of those electrons to the valence band of CIS [40]. The presence of MUA on the CIS can be confirmed by comparing the FTIR spectra of CIS and MUA. The disappearance of small region around 2680 cm^{-1} which corresponds to S–H stretching in the spectra of CIS confirms the bonding between MUA and CIS surface. Moreover, O–H stretch (broad region around 3000 cm^{-1}) and C]O stretch (sharp peak around 1720 cm^{-1}) in MUA [41] were cleaved in CIS. Therefore, it can be suggested that MUA capping ligand bonded to CIS surface not only by –SH group but also –COOH group interacted with CIS surface. Finally, C–H stretch (sharp peak around 2900 cm^{-1}) due to the alkene chain in MUA can be seen in both samples. The results have revealed that the increase in pH has led to improved solubility of MUA capped CIS quantum dots. The PL characteristic peak from radiative transmission signal was the highest at pH 9 which confirms the uniformly dispersed MUA capped CIS QDs. However, after pH 9, the PL signal decreased gradually and finally no characteristic peak was observed at pH 12.5–13 (Fig. S3). This will be discussed further.

The scanning electron microscopy (SEM) analysis showed that all obtained ZIS and ZIS/CIS photocatalysts are in microsphere shape which consists of many petals that results in microporous or mesoporous structure (Fig. 2a–e) as previously reported which is characteristic morphology for ZIS microspheres [13,17,32]. The size of all ZIS and ZIS/CIS range between 3 and 5 μm whereas thickness of the petals that form the microspheres are between 20 and 50 nm (Fig. 2a, b). The presence of CIS can be observed on all ZIS/CIS as aggregated form (Fig. 2b–e) probably due to the mercaptododecanoic acid

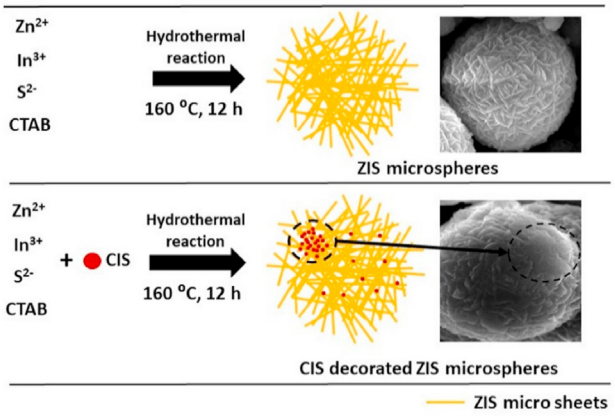

Fig. 1 – The synthesis route for ZIS and CIS decorated ZIS microspheres. Inset: SEM images of ZIS and ZIS/CIS.

anchored on CIS surface through not only thiol but also acid group (Fig. S2d) [42]. In addition to that, the acidic of reaction medium might cause decrease in electrostatic repulsion between MUA capped CIS which results in aggregation and nonuniformly distribution of CIS on ZIS surface [43]. On the other hand it was suggested that the better solubility of MUA capped CIS in water can be achieved at basic pH level in which the surface charge on MUA capped CIS increases due to the dissociation of carboxylic groups (Fig. S3) [44]. The increase in CIS on ZIS surface can be seen from the SEM images as in ZIS/CIS_200 (Fig. 2d), CIS covers most of the surface of ZIS while ZIS/CIS_50 (Fig. 2b) has lesser covered by CIS compared to ZIS/CIS_200 The scanning transmission electron microscope with high angle annular dark field (STEM-HAADF) imaging analysis showed the presence of CIS in ZIS which agrees with SEM results. Moreover, presence of CIS ranging between 1.8 and 2.4 nm (Fig. S2a, b) in accordance to comparison of STEM-HAADF images of ZIS/CIS_50 and ZIS/CIS_200. ZIS/CIS_50 has many gaps inside the between the layers of ZIS microspheres whereas these gaps diminishes in ZIS/CIS_200 which can be clearly seen by recognizable color change in the images due to the more situated CIS between the porous of ZIS/CIS_200 (Fig. 2j, t). In addition to STEM-HAADF, energy dispersive X-ray spectrometry (EDS) mapping approves the presence of CIS by measuring Cu element on ZIS/CIS photocatalyst and clearly reveals that CIS can be found in ZIS/CIS photocatalysts not only nonuniformly but also uniformly (Fig. 2n, s, x). The TEM images of the most active sample ZIS/CIS_100-Pt and without

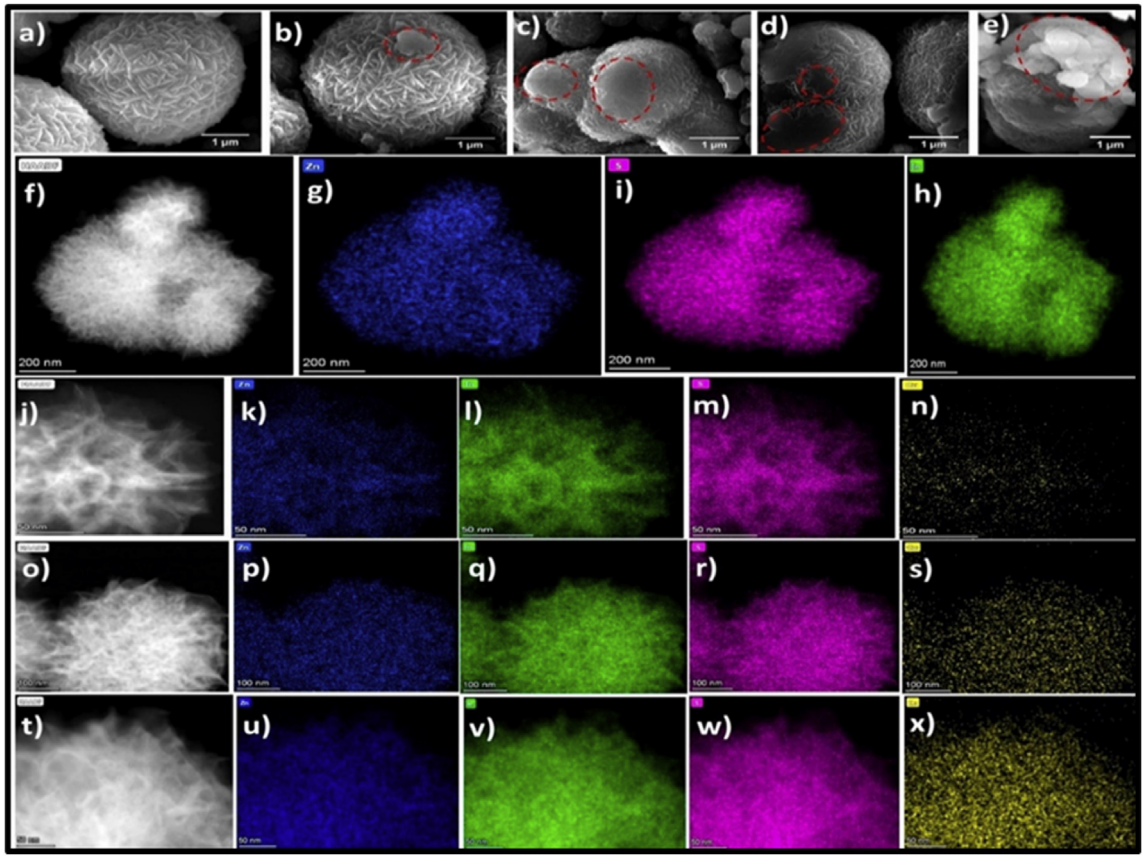

Fig. 2 – SEM images of a) ZIS, b) ZIS/CIS_50, c) ZIS/CIS_100, d) ZIS/CIS_150, e) ZIS/CIS_200 (dashed red circles show the aggregated CIS covering the ZIS surface), STEM-HAADF images of j) ZIS/CIS_50, o) ZIS/CIS_150, t) ZIS/CIS_200 with their EDS mapping of k), l), m), n) ZIS/CIS_50, p), q), r), s) ZIS/CIS_150, u), v), w), x) ZIS/CIS_200 (blue, green, purple and yellow colors represent Zn, In, S and Cu elements, respectively). (For interpretation of the references to color in this figure legend, the reader is referred to the Web version of this article.)

Pt deposition ZIS/CIS_100 was also compared (Fig. 3). The aggregated CIS with excess amount of MUA can be observed both in ZIS/CIS_100-Pt and ZIS/CIS_100 (Fig. 3a–c,e,f). Besides, the Pt based nanoparticles in forms of dark dots in the images with particle range around 13 nm can be observed in ZIS/CIS_100-Pt (Fig. 3d–f) sample differently from ZIS/CIS_100 (Fig. 3a–c) as expected. The X-ray diffraction (XRD) patterns of bare ZIS and ZIS/CIS exhibit same profile and any phase related with CIS were not detected due to the low crystallinity of CIS comparing to ZIS (Fig. S5a). XRD pattern of all ZIS/CIS, ZIS and CIS whereas Fig. S5b shows the detailed XRD spectra of CIS. All diffraction peaks of ZIS 20.65°, 28.1°, 28.5°, 47.4°, 51.8°, 56.3°, 69.2°, 76.5° and 88.4° were indexed to hexagonal crystal system in a sphalerite phase which are agreement with the literature [45,46] whereas peaks of CIS 27.5°,46.6°, 54.8° and 74.4° were indexed to tetragonal crystal system in a roquesite phase [39]. Moreover, the change in crystallography of ZIS-Pt and ZIS/CIS_100-Pt samples after four cycle of PHE performance experiment was also investigated by XRD (Fig. S6) and the newly formed 23.5°, 32.80°, 34.35°, 35.95°, 48.20°, 59.60° and 59.60° peaks which are indexed to trigonal structure of Na_2SO_3 [47] in the XRD spectra of both samples can be observed.

X-ray photoelectron spectroscopy (XPS) analysis identified all elements originated from ZIS and CIS (Fig. 4) and ZIS/CIS–Pt and evaluated the elemental surface composition of these heterostructures (Table S1). Different amount of CIS decorating ZIS were well controlled by atomic ratio Cu/Zn (Table S.1). The chemical nature of elements detected in ZIS/CIS–Pt (Zn, In, Cu, S and Pt) were determined by analysis of the high-resolution (HR) XPS spectra of Zn 2p, In 3d, Cu 2p, S 2p and Pt 4f, respectively (Tables S2 and S3). As a result, the oxidation states of Zn, In, Cu, and Pt was identified as Zn^{2+}, In^{3+}, Cu^{+}, and Pt^{2+}/Pt^{4+}, respectively (Tables S2 and S3). The resulted data are presented in Tables S2 and S3 and Fig. 2(a–e). The high-resolution (HR) XPS spectra of Zn 2p (a), In 3d(b), Cu 2p(c) and S 2p (d) agree well with the corresponding spectra reported in literature for ZIS/CIS nanocomposites [48–52]. The Zn 2p3/2 and In 3d5/2 peaks (BE of 1022.1 and 445.1 eV, respectively, Table S2) confirm the oxidation states of Zn^{2+} and In^{3+} in ZIS and CIS decorated ZIS heterostructures. The Cu 2p spectra features of MUA-capped CIS (c) identify Cu as Cu^{2+} state (Cu 2p3/2 signal at 932.7 eV accompanied by shakeup satellites at BE higher than 945.4 eV [53]). However, the Cu 2p spectra of all ZIS/CIS nanomaterials (Fig. 4c) exhibit the Cu 2p3/2 signals at 932.3 eV, what indicates the oxidation states of Cu to be closer to Cu^{+} [53]. The S 2p spectra of ZIS (d) are not affected by different amount of doped CIS (the main S2p3/2 signals at BE of 161.9 eV). Moreover, for all ZIS/CIS specimens we found a similar atomic ratio S/In close to 2 (2.16 ± 0.19, Table S1). The surface area of Pt deposited ZIS/CIS photocatalyst is also well characterized by the same set of Zn 2p, In 3d, Cu 2p and S 2p spectra (Fig. S7a–c, e). Additionally, the successful doping of Pt was confirmed by the Pt 4f spectrum (Fig. S7d). Unfortunately, the Pt 4f spectrum is overlapped with the Cu 3p and In 4p signals. Thus, deconvolution of this spectrum was necessary to separate the Pt signals and evaluate the Pt contents (Table S1). As a result, two Pt states, represented by Pt 4f7/2 signals at 72.7 eV and 74.9.9 eV, were distinguished. First, can be assigned to Pt^{2+} surface species (PtS, Pt-O_x) and second one to Pt^{4+} compounds (PtS_2, PtO_2) [54]. Also, the amount of the Pt in all photocatalysts were confirmed by ICP-OES that proves all the ZIS/CIS–Pt have about 1.26 wt% Pt (Table S.4).

Optical properties of ZIS/CIS, ZIS, CIS and ZIS/CIS–Pt were determined by UV–Vis diffusive reflectance spectroscopy (DRS) (Fig. S4a, b). The direct band gap value of ZIS [55] and CIS [26] were calculated by Kubelka-Munk method (Fig. S9)). CIS (1.87 eV) is more visible light responsive compare to all obtained ZIS (2.5 eV) and ZIS/CIS photocatalysts which has photoabsorption with the edge around more than 800 nm whereas ZIS, ZIS/CIS_50, ZIS/CIS_150 and ZIS/CIS_100, ZIS/CIS_200 are active with the edge about 630 nm and 660 nm, respectively (Fig. S4a). The color change in ZIS powder from

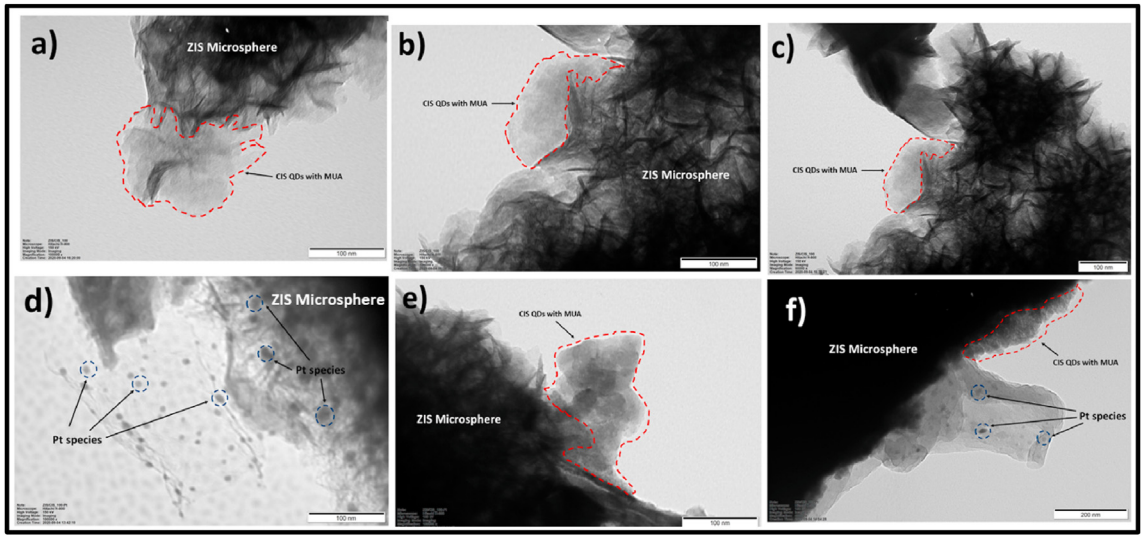

Fig. 3 – TEM images of a, b, c) ZIS/CIS_100 and d, e, f) ZIS/CIS_100-Pt. Red and blue dashed lines represents CIS QDs and Pt based particles, respectively. (For interpretation of the references to color in this figure legend, the reader is referred to the Web version of this article.)

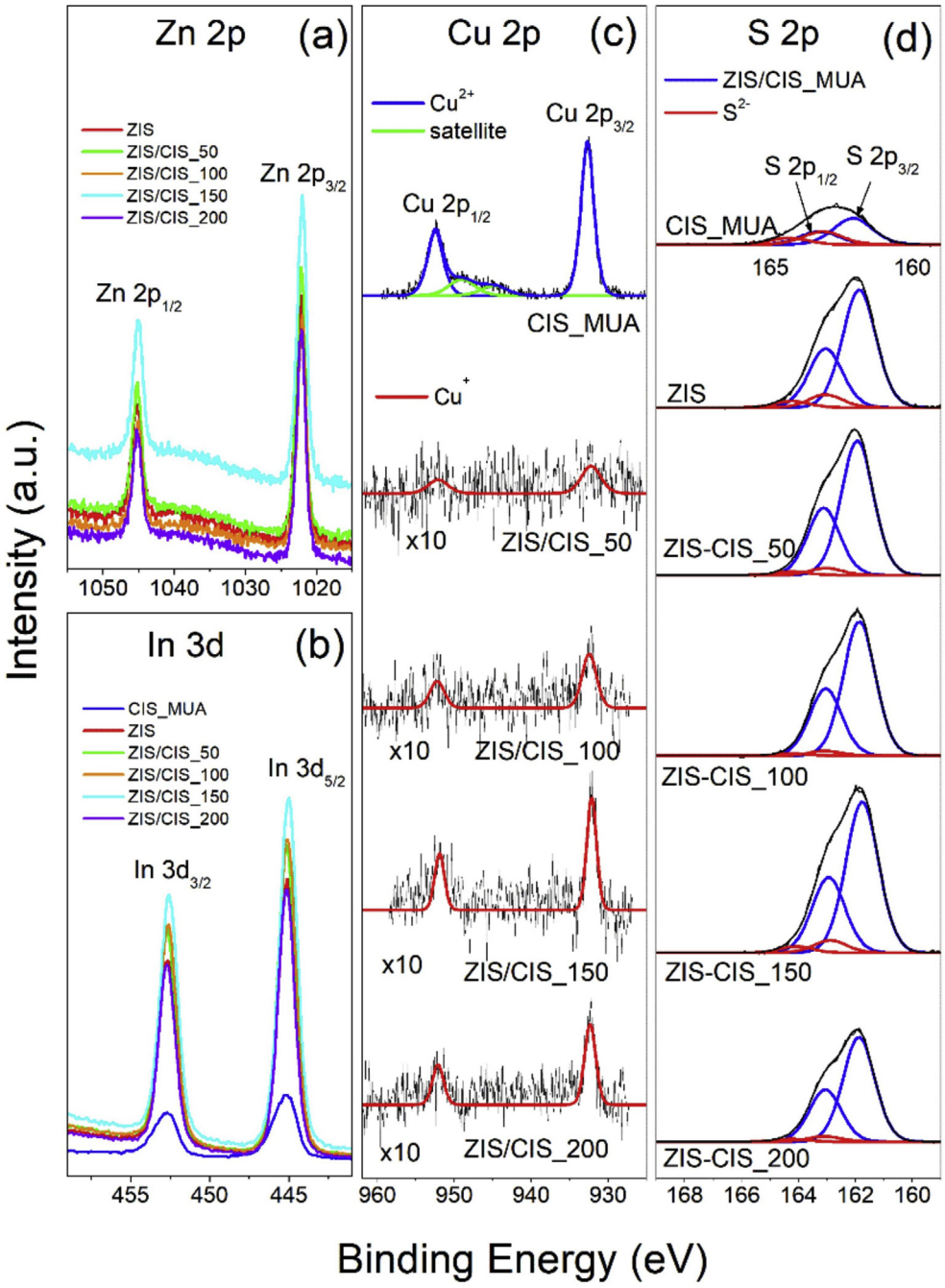

Fig. 4 – XPS spectra of a) Zn 2p, b) In 3d, c) Cu 2p, d) S 2p for ZIS/CIS and CIS with MUA samples.

yellow to reddish-yellow ZIS/CIS powders also confirms the slight increase of visible light absorption between 400 and 600 nm of ZIS/CIS compare to ZIS (Fig. S4a). After the Pt photodeposition on ZIS and ZIS/CIS surface, the significant increase in the absorption edge can be easily identified in all obtained photocatalysts which is much higher than of all ZIS/CIS (Fig. S4b). This enhancement can be explained by the increase in localized energy levels and surface plasmon resonance effect created by Pt nanoparticles on ZIS and ZIS-CIS surface [13,56,57]. Among ZIS/CIS–Pt photocatalysts, ZIS/CIS_100-Pt has the highest absorption while the lowest absorption can be observed in ZIS/CIS_50-Pt and ZIS/CIS_200-Pt. In order to investigate the recombination of photo-generated electron-hole on the surface of ZIS, ZIS/CIS and ZIS/CIS–Pt, photoluminescence (PL) spectra were studied by fluorescence spectrometry (FS) [32,58]. The lowest PL intensity detected in ZIS/CIS_100-Pt in comparison to all photocatalysts with and without Pt deposition which proves the lowest electron-hole recombination takes place in that photocatalyst. Meanwhile, ZIS/CIS_200 and ZIS/CIS_200-Pt exhibit highest PL (Fig. S4c, d) which reveals that ZIS/CIS_200-Pt (2.24 wt%) increases the recombination of hole-electrons. This increase might be explained due to the excessive amount of CIS on the ZIS surface leading to

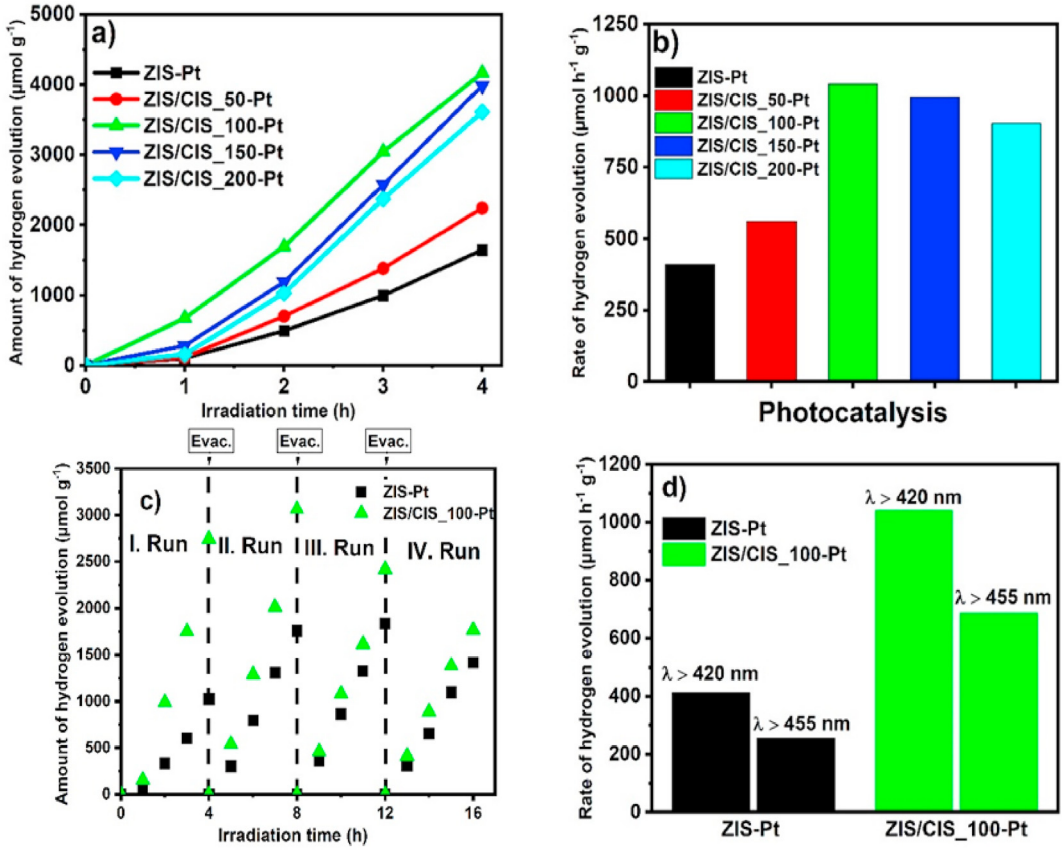

Fig. 5 – a) Amount and b) rate of hydrogen evolution under visible light irradiation (λ > 420) nm in the presence of ZIS-Pt and ZIS/CIS–Pt samples, c) cycling hydrogen evolution on ZIS-Pt and ZIS/CIS_100-Pt under visible light irradiation (λ > 455 nm) and d) comparison of rate of hydrogen evolution of ZIS-Pt and ZIS/CIS_100-Pt in the presence of GG420 (λ > 420 nm) and GG455 (λ > 455 nm) cut-off filters.

formation of recombination centers in connection with the narrow energy gap of CIS [59].

The amount of H_2 generated under visible light irradiation (λ > 420 nm) from Na_2S/Na_2SO_3 sacrifical agent solution by each ZIS/CIS–Pt after 4 h can be seen in Fig. 3a. All the ZIS/CIS–Pt photocatalysts have higher rate of H_2 than ZIS-Pt (Fig. 5b). The highest H_2 evolution rate of 1041 μmol h^{-1} g^{-1} is exhibited by ZIS/CIS_100-Pt which is about 2.5 times higher than that of ZIS-Pt (411.17 μmol h^{-1} g^{-1}). Thus, for the best PHE performance by ZIS/CIS can be reached with the ratio of 1.13 wt% of CIS. This hydrogen evolution rate is around 3.4 times lower compare to the 2D ZIS/CIS system with higher optimum amount of CIS (5 wt%) and Pt deposition (2 wt%) but also around 1.3 times higher than Cu doped ZIS with lower amount of Cu doping (0.5 wt%) and higher Pt deposition (1 wt%) (Table S5). Moreover, among ZIS/CIS–Pt, ZIS/CIS_50-Pt exhibits the lowest H_2 generation rate of 559.88 μmol h^{-1} g^{-1}. Above 1.13 wt% CIS, the PHE rate gradually decreases as is seen from the H_2 evolution rate of 995.27 and 902.07 μmol h^{-1} g^{-1} by ZIS/CIS_150-Pt (1.6 wt%) and ZIS/CIS_200-Pt (2.24 wt%), respectively (Fig. 5b). On the other hand, the photostability of ZIS/CIS_100-Pt and ZIS-Pt were investigated (Fig. 5c) under visible light irradiation (λ > 455 nm). ZIS/CIS_100-Pt and ZIS-Pt exhibit considerable H_2 evolution performance even at longer wavelength in the 1st run, 1025.26 and 2745.32 μmol g^{-1}. In the 2nd run, both samples show an increase in H_2 evolution, more particularly ZIS-Pt produced around 1.7 times higher H_2 (1760 μmol g^{-1}) than in 1st run. After the 2nd run, both samples show a gradual decrease in the amount of H_2 evolution. However, it is worth to mention that the amount of hydrogen evolution by ZIS-Pt after 4th run (1415.66 μmol g^{-1}) is still higher than that of its evolution amount in the end of 1st run while around 25% decrease can be observed from ZIS/CIS_100-Pt (1765.46 μmol g^{-1}) (Fig. 5c). Moreover, around 35% decrease in the rate of hydrogen evolution can be seen in the both ZIS-Pt and ZIS/CIS_100-Pt as the cut-off filter is changed from GG420 (λ > 420) nm to GG455 (λ > 455 nm) (Fig. 5d).

The mechanism of PHE of ZIS/CIS–Pt under visible light can be estimated firstly by approximating band structure of ZIS and CIS in accordance to valence band (VB) XPS spectra and calculated bandgap values from DRS. Based on this, the conduction band potential (E_{CB}) of CIS and ZIS can be determined [33,60,61]. Based on this, the valence band maximum values of ZIS and CIS are 1.5 eV and 0.6 eV (V vs NHE) (Fig. S8), whereas the direct bad gap (Eg) of ZIS and CIS were estimated by Kubelka-Munk function [62–65] using Eq. (2):

$$F(R).h\upsilon = k\,(h\upsilon - Eg)^{1/n} \quad (2)$$

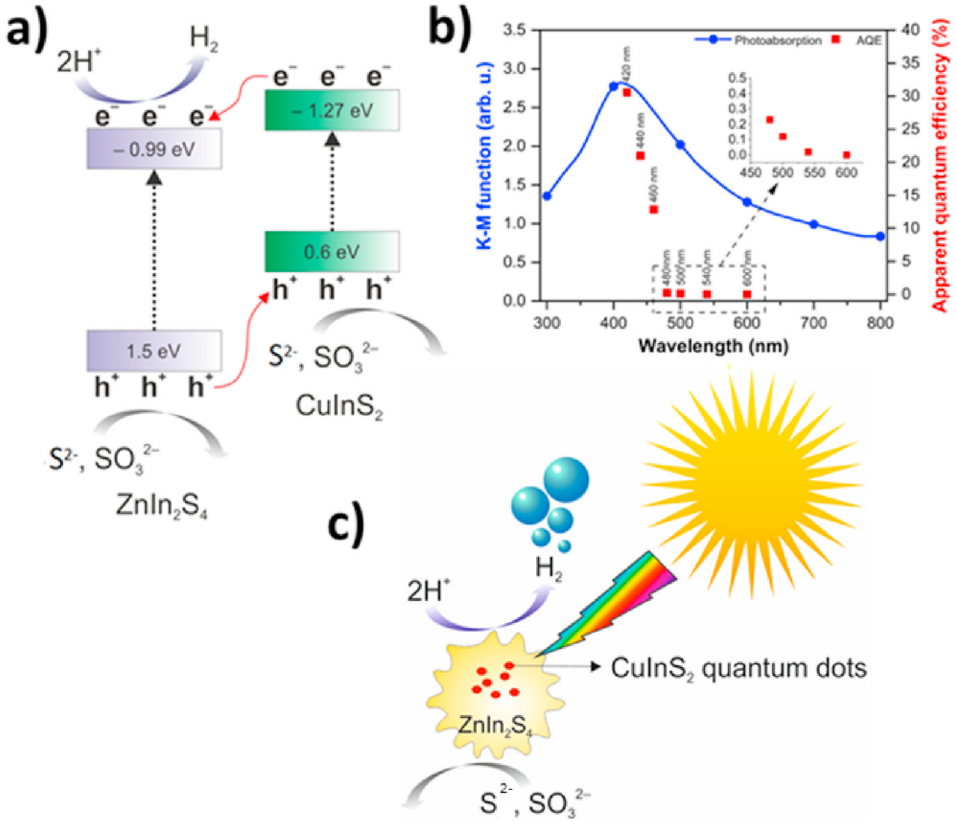

Fig. 6 – a) Charge transfer mechanism and band alignment in the ZIS/CIS–Pt (V vs NHE) b) action spectra analysis of photogenerated hydrogen evolution over ZIS/CIS_100-Pt sample c) schematic representation of photogenerated hydrogen evolution.

where F(R) is Kubelka-Munk function, R is the reflectance (Fig. S9) and n is the exponent depending the on type of transition which is n = 2 for both ZIS and CIS. By using the plot of $(F(R).\ hv)^2$ vs. hv., Eg of CIS and ZIS are about Eg = 1.87 and 2.49 eV, respectively. Finally, by considering the Eg and E_{VB}, the conduction band (CB) of ZIS and CIS was estimated around −0.99 and −1.27 eV (V vs NHE), respectively. Thus, the CB potentials of both ZIS and CIS are thermodynamically suitable for PHE by considering the H^+/H_2 reduction potential 0 eV (V vs NHE) [32]. During the visible light irradiation, ZIS and CIS are photoexcited and produces photogenerated electron (e^-) and holes (h^+). The photogenerated electrons on the CIS surface move to lower CB potential of ZIS and are captured by active sites of ZIS/CIS–Pt where Pt nanoparticles acting as an electron sink for H_2 generation by capturing the photogenerated electrons and prevent the recombination [66,67]. Meanwhile, photogenerated holes in ZIS are captured by the VB of CIS that results in inhibition of recombination of holes and electrons on ZIS and the holes on CIS surface are scavenged by SO_3^{2-} and S^{2-} ions to form SO_4^{2-} and S_2^{2-}, respectively. So that the charge separation over ZIS/CIS–Pt surface is facilitated [68,69] (Fig. 6a, c). Moreover, it is worth to mention that the rise in PHE rate of ZIS/CIS_100-Pt might be associated with the adsorption mechanism on the photocatalysis surface [70]. In more detail, the photogenerated electrons and holes-initiated reactions are given below on the photocatalysis surface in the case of Na_2S/Na_2SO_3 sacrificial agent solution [71].

$$2H_2O + 2e^- \rightarrow H_2 + 2OH^- \quad \text{(I)}$$

$$SO_3^{2-} + 2H_2O + 2h^+ \rightarrow SO_4^{2-} + 2H^+ \quad \text{(II)}$$

$$2S^{2-} + 2h^+ \rightarrow S_2^{2-} \quad \text{(III)}$$

$$S_2^{2-} + SO_3^{2-} \rightarrow S_2O_3^{2-} + S^{2-} \quad \text{(IV)}$$

$$SO_3^{2-} + S^{2-} + 2h^+ \rightarrow S_2O_3^{2-} \quad \text{(V)}$$

After charge carrier generation, photogenerated holes-initiated reactions occur and SO_3^{2-} and S^{2-} ions form SO_4^{2-} and S_2^{2-} ions, respectively. However, initial condition for these surface reactions is competitive adsorption of Na_2SO_3 and Na_2S on photocatalysis surface which follows Langmuir-Hinshelwood model [72]. Therefore, the higher surface area in ZIS/CIS_100-Pt (32.5 m^2/g) comparing to ZIS-Pt (24 m^2/g) might lead to more Na_2SO_3 consumption on its surface thus higher PHE rate. Consequently, the optimum amount of CIS (1.13 wt%) in ZIS/CIS photocatalyst increases the charge separation efficiently by forming a heterojunction that leads to enhancement of the PHE rate comparing to bare ZIS. To gain

insight into the mechanism of photocatalytic hydrogen evolution, the action spectra analysis was performed with ZIS/CIS_100-Pt and apparent quantum efficiency (AQE) was calculated as a function of the irradiation light (420, 440, 460, 480, 500, 540 and 600 nm). Indeed, the ZIS/CIS_100-Pt sample had high ability to generate H_2 in the visible light range up to a wavelength of 540 nm, which correlates well with its photoabsorption properties – less light absorption capacity led to less H_2 evolution and lower AQE values (Fig. 6b). For the longer wavelength than 540 nm (600 nm), AQE reached the values of 0%. In addition, two regions can be distinguished, namely with extremely high (up to 480 nm) and moderate (from 480 to 540 nm) power to evaluate H_2. The highest AQE was observed at 420 nm (30.6%). To the best of our knowledge this value is second the highest results among the $ZnIn_2S_4$–based photocatalysts in the literature (Table S5) and the widest region with observable H_2 evolution photoactivity. Thus, photocatalytic H_2 evolution was mainly dependent on the photoabsorption properties of the ZIS/CIS photocatalyst. As very low activity was exhibited by both ZIS and CIS without Pt deposition (Fig. S10), the effect of the Pt species on photogenerated hydrogen evolution rate can be expected. In consideration of Pt oxides, Pt-Ox and PtO_2, it was suggested that maximization of Pt^{4+} sites are more efficient than that of Pt^{2+} species in electrochemical hydrogen evolution [73]. However, in the case of Pt sulfides, PtS and PtS_2, this might be different. During photodeposition process, excessive amount of sulfur in $ZnIn_2S_4$ promotes more likely the formation of PtS semiconductor on $ZnIn_2S_4$ due to the adsorption of Pt^{2+} on $ZnIn_2S_4$ [74]. The same phenomena might occur in ZIS/CIS_100-Pt and ZIS/CIS–Pt samples as is seen from previously mentioned XPS results that Pt^{2+} state can be detected in ZIS/CIS_100-Pt and ZIS/CIS–Pt surface. However, Pt^{4+} was also detected which corresponds according to PtO_2 or PtS_2 species in ZIS/CIS_100-Pt and ZIS/CIS–Pt samples according to the XPS results. The increased Pt(II) component contribution by reduction of PtS_2 resulted in induced the hydrogen evolution rate in PtS_2 [75]. Moreover it was also reported that PtS_x worked more efficiently than the metallic Pt particles in case of Z-scheme employing metal sulfide photocatalysis [76]. As a result, one can suggest that different species of Pt have different activity: in case of Pt oxides, PtO_2 > Pt-Ox whereas for Pt sulfides PtS > PtS_2 among Pt sulfides. However detailed studies are crucial to reveal which form of those species exist dominantly in ZIS/CIS_100-Pt and ZIS/CIS–Pt samples. On the other hand, the decrease in H_2 generation rate above the optimum amount of CIS can be also highlighted. Above the optimum value of CIS, as clearly seen in Fig. 1e, the ZIS surface is covered by CIS in which the photons required for photoexcitation of ZIS might be blocked. Therefore, photoexcitation of ZIS diminishes due to the insufficient number of photons reaching ZIS surface. Thereby, induced the number of photoexcited electrons and holes results in a drop of PHE rate. Also, in higher amounts, CIS may locate the active sites in ZIS for H_2 generation [77] and creates recombination centers competing with the active sites for H_2 evolution and increases the recombination rate (Fig. S4d). Moreover, over CIS decoration than the optimum might narrow the space charge region in ZIS/CIS heterojunction system, and the penetration depth of ZIS surpasses the space charge layer in which photogenerated holes and electrons recombine easier [78]. In addition, the rapid decline in photocatalytic activity in both ZIS-Pt and ZIS/CIS_100-Pt samples after the 2nd run can be linked to the self-oxidation of S^{2-} in ZIS by photo-generated holes in the valence band of ZIS [52]. That is supported by XPS results of both ZIS-Pt and ZIS/CIS_100-Pt samples before and after cycling experiments in which remarkable drop can be seen in fraction of S^{2-} state (Table S3). Furthermore, that decline can be also correlated to the notable decrease in Zn and In contents in ZIS-Pt and ZIS/CIS_100-Pt samples (Fig. S7 and Table S1 and S3). However, the XPS peak related with Cu 3p orbital decreased also in ZIS/CIS_100-Pt sample after photostability cycle runs, but this decrease is not significant as in Zn and In contents (Fig. S7).

Conclusions

$ZnIn_2S_4$ microspheres decorated with pre-prepared $CuInS_2$ quantum dots were prepared successfully by simple hydrothermal reaction and modified by Pt photodeposition for the first time. Introducing optimum amount of 1.13 wt% $CuInS_2$ quantum dots to the hydrothermal reaction medium for $ZnIn_2S_4$ microspheres increased rate of bare ZIS about 2.5 times under visible light irradiation. This enhancement is related with the improved light harvesting ability of $ZnIn_2S_4$ microspheres/$CuInS_2$ quantum dots system in consequence of the formed heterojunction between $CuInS_2$ quantum dots and $ZnIn_2S_4$ matrix. The broad visible range photoactivity up to 540 nm was observed with remarkable AQE at 420 nm (30.6%). Further investigations are required to understand the fate of the quantum dots during hydrothermal reaction, the effect of the different reaction conditions on configuration of quantum dots on $ZnIn_2S_4$ matrixes and impact on photocatalytic activity. Moreover, the optimum amount of Pt deposition on $ZnIn_2S_4$ microspheres/$CuInS_2$ quantum dots heterojunction system must be investigated for the further studies. We suggest that using $CuInS_2$ quantum dots as a reactant in a hydrothermal synthesis can be an alternative approach to obtain heterojunction to improve the photocatalytic activity of $ZnIn_2S_4$ for photogenerated hydrogen evolution applications.

Declaration of competing interest

The authors declare that they have no known competing financial interests or personal relationships that could have appeared to influence the work reported in this paper.

Acknowledgement

This research was financially supported by National Science Centre, Poland (Grant No. 2016/23/D/ST8/02682). Action spectra set-up was financially support by National Science Centre, Poland (Grant No. 2016/23/B/ST8/03336). We would like to thank Lothar Houben from Weizmann Institute of Science for STEM-HAADF images and Andrzej Żak from Wrocław University of Science and Technology for TEM images of ZIS/CIS_100 and ZIS/CIS_100-Pt samples.

Appendix A. Supplementary data

Supplementary data to this article can be found online at https://doi.org/10.1016/j.ijhydene.2020.09.212.

REFERENCES

[1] Dutta S. A review on production, storage of hydrogen and its utilization as an energy resource. J Ind Eng Chem 2014;20:1148–56. https://doi.org/10.1016/j.jiec.2013.07.037.

[2] Edwards PP, Kuznetsov VL, David WIF, Brandon NP. Hydrogen and fuel cells: towards a sustainable energy future. Energy Pol 2008;36:4356–62. https://doi.org/10.1016/j.enpol.2008.09.036.

[3] Dincer I, Acar C. Review and evaluation of hydrogen production methods for better sustainability. Int J Hydrogen Energy 2014;40:11094–111. https://doi.org/10.1016/j.ijhydene.2014.12.035.

[4] Fujishima A, Honda K. Electrochemical photolysis of water at a semiconductor electrode. Nature 1972;238:37–8. https://doi.org/10.1038/238037a0.

[5] Yang X, Xue H, Xu J, Huang X, Zhang J, Tang YB, Ng TW, Kwong HL, Meng XM, Lee CS. Synthesis of porous ZnS:Ag2S nanosheets by ion exchange for photocatalytic H2 generation. ACS Appl Mater Interfaces 2014;6:9078–84. https://doi.org/10.1021/am5020953.

[6] Liu Z, Bai H, Xu S, Sun DD. Hierarchical CuO/ZnO "corn-like" architecture for photocatalytic hydrogen generation. Int J Hydrogen Energy 2011;36:13473–80. https://doi.org/10.1016/j.ijhydene.2011.07.137.

[7] Bai H, Juay J, Liu Z, Song X, Lee SS, Sun DD. Hierarchical SrTiO 3/TiO 2 nanofibers heterostructures with high efficiency in photocatalytic H 2 generation. Appl Catal B Environ 2012;125:367–74. https://doi.org/10.1016/j.apcatb.2012.06.007.

[8] Gasparotto A, Barreca D, Bekermann D, Devi A, Fischer RA, Fornasiero P, Gombac V, Lebedev OI, MacCato C, Montini T, Van Tendeloo G, Tondello E. F-doped Co3O4 photocatalysts for sustainable H 2 generation from water/ethanol. J Am Chem Soc 2011;133:19362–5. https://doi.org/10.1021/ja210078d.

[9] Tijare SN, Joshi MV, Padole PS, Mangrulkar PA, Rayalu SS, Labhsetwar NK. Photocatalytic hydrogen generation through water splitting on nano-crystalline LaFeO3 perovskite. Int J Hydrogen Energy 2012;37:10451–6. https://doi.org/10.1016/j.ijhydene.2012.01.120.

[10] Marschall R, Soldat J, Wark M. Enhanced photocatalytic hydrogen generation from barium tantalate composites. Photochem Photobiol Sci 2013;12:671–7. https://doi.org/10.1039/c2pp25200g.

[11] Khan Z, Qureshi M. Tantalum doped BaZrO3 for efficient photocatalytic hydrogen generation by water splitting. Catal Commun 2012;28:82–5. https://doi.org/10.1016/j.catcom.2012.08.002.

[12] Lozano-Sánchez LM, Méndez-Medrano MG, Colbeau-Justin C, Rodríguez-López JL, Hernández-Uresti DB, Obregón S. Long-lived photoinduced charge-carriers in Er3+ doped CaTiO3 for photocatalytic H2 production under UV irradiation. Catal Commun 2016;84:36–9. https://doi.org/10.1016/j.catcom.2016.06.002.

[13] Li Q, Cui C, Meng H, Yu J. Visible-light photocatalytic hydrogen production activity of ZnIn 2S4 microspheres using carbon quantum dots and platinum as dual co-catalysts. Chem - An Asian J 2014;9:1766–70. https://doi.org/10.1002/asia.201402128.

[14] Lei Z, You W, Liu M, Zhou G, Takata T, Hara M, Domen K, Li C. Photocatalytic water reduction under visible light on a novel ZnIn2S4 catalyst synthesized by hydrothermal method. Chem Commun 2003;3:2142–3. https://doi.org/10.1039/b306813g.

[15] Zhang S, Liu X, Liu C, Luo S, Wang L, Cai T, Zeng Y, Yuan J, Dong W, Pei Y, Liu Y. MoS 2 quantum dot growth induced by S vacancies in a ZnIn 2 S 4 monolayer: atomic-level heterostructure for photocatalytic hydrogen production. ACS Nano 2018;12:751–8. https://doi.org/10.1021/acsnano.7b07974.

[16] Gou X, Cheng F, Shi Y, Zhang L, Peng S, Chen J, Shen P. Shape-controlled synthesis of ternary chalcogenide Znln2S 4 and Culn(S,Se)2 nano-/microstructures via facile solution route. J Am Chem Soc 2006;128:7222–9. https://doi.org/10.1021/ja0580845.

[17] Shen S, Zhao L, Zhou Z, Guo L. Enhanced photocatalytic hydrogen evolution over Cu-doped ZnIn 2S4 under visible light irradiation. J Phys Chem C 2008;112:16148–55. https://doi.org/10.1021/jp804525q.

[18] Xia Y, Li Q, Lv K, Tang D, Li M. Superiority of graphene over carbon analogs for enhanced photocatalytic H2-production activity of ZnIn2S4. Appl Catal B Environ 2017;206:344–52. https://doi.org/10.1016/j.apcatb.2017.01.060.

[19] Zhu R, Tian F, Yang R, He J, Zhong J, Chen B. Z scheme system ZnIn2S4/RGO/BiVO4 for hydrogen generation from water splitting and simultaneous degradation of organic pollutants under visible light. Renew Energy 2019;139:22–7. https://doi.org/10.1016/j.renene.2019.02.049.

[20] Zeng D, Xiao L, Ong WJ, Wu P, Zheng H, Chen Y, Peng DL. Hierarchical ZnIn2S4/MoSe2 nanoarchitectures for efficient noble-metal-free photocatalytic hydrogen evolution under visible light. ChemSusChem 2017;10:4624–31. https://doi.org/10.1002/cssc.201701345.

[21] Liu H, Jin Z, Xu Z, Zhang Z, Ao D. Fabrication of ZnIn2S4-g-C3N4 sheet-on-sheet nanocomposites for efficient visible-light photocatalytic H2-evolution and degradation of organic pollutants. RSC Adv 2015;5:97951–61. https://doi.org/10.1039/c5ra17028a.

[22] Ye L, Wen Z. ZnIn2 S4 nanosheets decorating WO 3 nanorods core-shell hybrids for boosting visible-light photocatalysis hydrogen generation. Int J Hydrogen Energy 2019;44:3751–9. https://doi.org/10.1016/j.ijhydene.2018.12.093.

[23] Bozetine H, Wang Q, Barras A, Li M, Hadjersi T, Szunerits S, Boukherroub R. Green chemistry approach for the synthesis of ZnO-carbon dots nanocomposites with good photocatalytic properties under visible light. J Colloid Interface Sci 2016;465:286–94. https://doi.org/10.1016/j.jcis.2015.12.001.

[24] Kumar S, Dhiman A, Sudhagar P, Krishnan V. ZnO-graphene quantum dots heterojunctions for natural sunlight-driven photocatalytic environmental remediation. Appl Surf Sci 2018;447:802–15. https://doi.org/10.1016/j.apsusc.2018.04.045.

[25] Li Y, Lv K, Ho W, Dong F, Wu X, Xia Y. Hybridization of rutile TiO2 (rTiO2) with g-C3N4 quantum dots (CN QDs): an efficient visible-light-driven Z-scheme hybridized photocatalyst. Appl Catal B Environ 2017;202:611–9. https://doi.org/10.1016/j.apcatb.2016.09.055.

[26] Shen F, Que W, Liao Y, Yin X. Photocatalytic activity of TiO2 nanoparticles sensitized by CuInS2 quantum dots. Ind Eng Chem Res 2011;50:9131–7. https://doi.org/10.1021/ie2007467.

[27] Wang K, Zhang G, Li J, Li Y, Wu X. 0D/2D Z-scheme heterojunctions of bismuth tantalate quantum dots/ultrathin g-C 3 N 4 nanosheets for highly efficient visible light photocatalytic degradation of antibiotics. ACS Appl Mater Interfaces 2017;9:43704–15. https://doi.org/10.1021/acsami.7b14275.

[28] Ge L, Zuo F, Liu J, Ma Q, Wang C, Sun D, Bartels L, Feng P. Synthesis and efficient visible light photocatalytic hydrogen evolution of Polymeric g-C 3N 4 coupled with CdS quantum dots. J Phys Chem C 2012;116:13708–14. https://doi.org/10.1021/jp3041692.
[29] Bera D, Qian L, Tseng TK, Holloway PH. Quantum dots and their multimodal applications: a review. Materials 2010;3:2260–345. https://doi.org/10.3390/ma3042260 (Basel).
[30] Frigerio C, Ribeiro DSM, Rodrigues SSM, Abreu VLRG, Barbosa JAC, Prior JAV, Marques KL, Santos JLM. Application of quantum dots as analytical tools in automated chemical analysis: a review. Anal Chim Acta 2012;735:9–22. https://doi.org/10.1016/j.aca.2012.04.042.
[31] Bajorowicz B, Kobylański MP, Gołąbiewska A, Nadolna J, Zaleska-Medynska A, Malankowska A. Quantum dot-decorated semiconductor micro- and nanoparticles: a review of their synthesis, characterization and application in photocatalysis. Adv Colloid Interface Sci 2018;256:352–72. https://doi.org/10.1016/j.cis.2018.02.003.
[32] Hou J, Yang C, Cheng H, Wang Z, Jiao S, Zhu H. Ternary 3D architectures of CdS QDs/graphene/ZnIn2S4 heterostructures for efficient photocatalytic H2 production. Phys Chem Chem Phys 2013;15:15660–8. https://doi.org/10.1039/c3cp51857d.
[33] Zhang S, Wang L, Liu C, Luo J, Crittenden J, Liu X, Cai T, Yuan J, Pei Y, Liu Y. Photocatalytic wastewater purification with simultaneous hydrogen production using MoS2 QD-decorated hierarchical assembly of ZnIn2S4 on reduced graphene oxide photocatalyst. Water Res 2017;121:11–9. https://doi.org/10.1016/j.watres.2017.05.013.
[34] Sandroni M, Gueret R, Wegner KD, Reiss P, Fortage J, Aldakov D, Collomb MN. Cadmium-free CuInS2/ZnS quantum dots as efficient and robust photosensitizers in combination with a molecular catalyst for visible light-driven H2 production in water. Energy Environ Sci 2018;11:1752–61. https://doi.org/10.1039/c8ee00120k.
[35] Hu W, Yang S, Huang J. Composition effect on the carrier dynamics and catalytic performance of CuInS2/ZnS quantum dots for light driven hydrogen generation. J Chem Phys 2019;151. https://doi.org/10.1063/1.5125024.
[36] Nie C, Ni W, Gong L, Jiang J, Wang J, Wang M. Charge transfer dynamics and catalytic performance of a covalently linked hybrid assembly comprising a functionalized cobalt tetraazamacrocyclic catalyst and CuInS2/ZnS quantum dots for photochemical hydrogen production. J Mater Chem A 2019;7:27432–40. https://doi.org/10.1039/c9ta10479h.
[37] Guan Z, Pan J, Li Q, Li G, Yang J. Boosting visible-light photocatalytic hydrogen evolution with an efficient CuInS 2/ZnIn 2 S 4 2D/2D heterojunction. ACS Sustain Chem Eng 2019;7:7736–42. https://doi.org/10.1021/acssuschemeng.8b06587.
[38] Guo X, Peng Y, Liu G, Xie G, Guo Y, Zhang Y, Yu J. An efficient ZnIn 2 S 4 @CuInS 2 core–shell p–n heterojunction to boost visible-light photocatalytic hydrogen evolution. J Phys Chem C 2020;124:5934–43. https://doi.org/10.1021/acs.jpcc.9b11623.
[39] Booth M. Synthesis and characterisation of CuInS2 quantum dots. The University of Leeds School of Physics & Astronomy; 2014. https://doi.org/uk.bl.ethos.640628.
[40] Lim J, Bae WK, Kwak J, Lee S, Lee C, Char K. Perspective on synthesis, device structures, and printing processes for quantum dot displays. Opt Mater Express 2012;2:594. https://doi.org/10.1364/ome.2.000594.
[41] Simsikova M, Antalík M, Kaňuchová M, Škvarla J. Anionic 11-mercaptoundecanoic acid capped ZnO nanoparticles. Appl Surf Sci 2013;282:342–7. https://doi.org/10.1016/j.apsusc.2013.05.130.
[42] Kim H, Suh M, Kwon BH, Jang DS, Kim SW, Jeon DY. In situ ligand exchange of thiol-capped CuInS2/ZnS quantum dots at growth stage without affecting luminescent characteristics. J Colloid Interface Sci 2011;363:703–6. https://doi.org/10.1016/j.jcis.2011.06.087.
[43] Algar WR, Krull UJ. Luminescence and stability of aqueous thioalkyl acid capped CdSe/ZnS quantum dots correlated to ligand ionization. ChemPhysChem 2007;8:561–8. https://doi.org/10.1002/cphc.200600686.
[44] Hardzei M, Artemyev M. Influence of pH on luminescence from water-soluble colloidal Mn-doped ZnSe quantum dots capped with different mercaptoacids. J Lumin 2012;132:425–8. https://doi.org/10.1016/j.jlumin.2011.09.018.
[45] Shen S, Zhao L, Guo L, Crystallite. Optical and photocatalytic properties of visible-light-driven ZnIn2S4 photocatalysts synthesized via a surfactant-assisted hydrothermal method. Mater Res Bull 2009;44:100–5. https://doi.org/10.1016/j.materresbull.2008.03.027.
[46] Tian F, Zhu R, Song K, Niu M, Ouyang F, Cao G. The effects of hydrothermal temperature on the photocatalytic performance of ZnIn2S4 for hydrogen generation under visible light irradiation. Mater Res Bull 2015;70:645–50. https://doi.org/10.1016/j.materresbull.2015.05.033.
[47] Jain A, Ong SP, Hautier G, Chen W, Richards WD, Dacek S, Cholia S, Gunter D, Skinner D, Ceder G, Persson KA. Commentary: the materials project: a materials genome approach to accelerating materials innovation. Apl Mater 2013;1. https://doi.org/10.1063/1.4812323.
[48] De Trizio L, Prato M, Genovese A, Casu A, Povia M, Simonutti R, Alcocer MJP, D'Andrea C, Tassone F, Manna L. Strongly fluorescent quaternary Cu-In-Zn-S nanocrystals prepared from Cu 1-xInS 2 nanocrystals by partial cation exchange. Chem Mater 2012;24:2400–6. https://doi.org/10.1021/cm301211e.
[49] Tang X, Tay Q, Chen Z, Chen Y, Goh GKL, Xue J. CuInZnS-decorated graphene nanosheets for highly efficient visible-light-driven photocatalytic hydrogen production. J Mater Chem A 2013;1:6359–65. https://doi.org/10.1039/c3ta01602a.
[50] Gabka G, Bujak P, Giedyk K, Kotwica K, Ostrowski A, Malinowska K, Lisowski W, Sobczak JW, Pron A. Ligand exchange in quaternary alloyed nanocrystals - a spectroscopic study. Phys Chem Chem Phys 2014;16:23082–8. https://doi.org/10.1039/c4cp03850a.
[51] Courtel FM, Paynter RW, Marsan B, Morin M. Synthesis, characterization, and growth mechanism of n-Type CuInS 2 colloidal particles. Chem Mater 2009;21:3752–62. https://doi.org/10.1021/cm900601k.
[52] Do JY, Choi S, Nahm K, Kim SK, Kang M. Reliable hydrogen production from methanol photolysis in aqueous solution by a harmony between in and Zn in bimetallic zinc indium sulfide. Mater Res Bull 2018;100:234–42. https://doi.org/10.1016/j.materresbull.2017.12.034.
[53] Biesinger MC, Lau LWM, Gerson AR, Smart RSC. Resolving surface chemical states in XPS analysis of first row transition metals, oxides and hydroxides: Sc, Ti, V, Cu and Zn. Appl Surf Sci 2010;257:887–98. https://doi.org/10.1016/j.apsusc.2010.07.086.
[54] Naumkin AV, Kraut-Vass A, Gaarenstroom SW, Powell CJ. NIST X-ray photoelectron spectroscopy database, NIST standard reference database 20. Natl. Inst. Stand. Technol.; 2012. https://doi.org/10.18434/T4T88K., Version 4.1.
[55] Wang G, Chen G, Yu Y, Zhou X, Teng Y. Mixed solvothermal synthesis of hierarchical ZnIn2S4 spheres: specific facet-induced photocatalytic activity enhancement and a DFT elucidation. RSC Adv 2013;3:18579–86. https://doi.org/10.1039/c3ra42245c.
[56] Sakthivel S, Shankar MV, Palanichamy M, Arabindoo B, Bahnemann DW, Murugesan V. Enhancement of photocatalytic activity by metal deposition: characterisation and photonic efficiency of Pt, Au and Pd deposited on TiO 2

catalyst. Water Res 2004;38:3001–8. https://doi.org/10.1016/j.watres.2004.04.046.
[57] Vamvasakis I, Liu B, Armatas GS. Size effects of platinum nanoparticles in the photocatalytic hydrogen production over 3D mesoporous networks of CdS and Pt nanojunctions. Adv Funct Mater 2016;26:8062–71. https://doi.org/10.1002/adfm.201603292.
[58] Wang Z, Hou J, Jiao S, Huang K, Zhu H. In situ chemical reduction of the Ta 3N 5 quantum dots coupled TaON hollow spheres heterojunction photocatalyst for water oxidation. J Mater Chem 2012;22:21972–8. https://doi.org/10.1039/c2jm35374a.
[59] Li X, Wang J, Men Y, Bian Z. TiO2 mesocrystal with exposed (001) facets and CdS quantum dots as an active visible photocatalyst for selective oxidation reactions. Appl Catal B Environ 2016;187:115–21. https://doi.org/10.1016/j.apcatb.2016.01.034.
[60] Zhou X, Wierzbicka E, Liu N, Schmuki P. Black and white anatase, rutile and mixed forms: band-edges and photocatalytic activity. Chem Commun 2019;55:533–6. https://doi.org/10.1039/c8cc07665k.
[61] Xu J, Teng Y, Teng F. Effect of surface defect states on valence band and charge separation and transfer efficiency. Sci Rep 2016;6:1–9. https://doi.org/10.1038/srep32457.
[62] Köferstein R, Jäger L, Ebbinghaus SG. Magnetic and optical investigations on LaFeO3 powders with different particle sizes and corresponding ceramics. Solid State Ionics 2013;249–250:1–5. https://doi.org/10.1016/j.ssi.2013.07.001.
[63] Köferstein R, Ebbinghaus SG. Investigations of BaFe0.5Nb0.5O3 nano powders prepared by a low temperature aqueous synthesis and resulting ceramics. J Eur Ceram Soc 2017;37:1509–16. https://doi.org/10.1016/j.jeurceramsoc.2016.12.014.
[64] López R, Gómez R. Band-gap energy estimation from diffuse reflectance measurements on sol-gel and commercial TiO 2: a comparative study. J Sol-Gel Sci Technol 2012;61:1–7. https://doi.org/10.1007/s10971-011-2582-9.
[65] Nowak M, Kauch B, Szperlich P. Determination of energy band gap of nanocrystalline SbSI using diffuse reflectance spectroscopy. Rev Sci Instrum 2009;80:21–4. https://doi.org/10.1063/1.3103603.
[66] Shen J, Zai J, Yuan Y, Qian X. 3D hierarchical ZnIn 2S 4: the preparation and photocatalytic properties on water splitting. Int J Hydrogen Energy 2012;37:16986–93. https://doi.org/10.1016/j.ijhydene.2012.08.038.
[67] Malankowska A, Kobylański MP, Mikolajczyk A, Cavdar O, Nowaczyk G, Jarek M, Lisowski W, Michalska M, Kowalska E, Ohtani B, Zaleska-Medynska A. TiO 2 and NaTaO 3 decorated by trimetallic Au/Pd/Pt core-shell nanoparticles as efficient photocatalysts: experimental and computational studies. ACS Sustain Chem Eng 2018;6:16665–82. https://doi.org/10.1021/acssuschemeng.8b03919.
[68] Wang L, Wang W, Shang M, Yin W, Sun S, Zhang L. Enhanced photocatalytic hydrogen evolution under visible light over Cd1-xZnxS solid solution with cubic zinc blend phase. Int J Hydrogen Energy 2010;35:19–25. https://doi.org/10.1016/j.ijhydene.2009.10.084.
[69] Mahadik MA, Shinde PS, Cho M, Jang JS. Fabrication of a ternary CdS/ZnIn2S4/TiO2 heterojunction for enhancing photoelectrochemical performance: effect of cascading electron-hole transfer. J Mater Chem A 2015;3:23597–606. https://doi.org/10.1039/c5ta07454a.
[70] Tambago HMG, de Leon RL. Intrinsic kinetic modeling of hydrogen production by photocatalytic water splitting using cadmium zinc sulfide catalyst. Int. J. Chem. Eng. Appl. 2015;6:220–7. https://doi.org/10.7763/ijcea.2015.v6.485.
[71] Bao N, Shen L, Takata T, Domen K. Self-templated synthesis of nanoporous CdS nanostructures for highly efficient photocatalytic hydrogen production under visible light. Chem Mater 2008;20:110–7. https://doi.org/10.1021/cm7029344.
[72] Markovskaya DV, Cherepanova SV, Saraev AA, Gerasimov EY, Kozlova EA. Photocatalytic hydrogen evolution from aqueous solutions of Na2S/Na2SO3 under visible light irradiation on CuS/Cd0.3Zn0.7S and NizCd0.3Zn0.7S1+z. Chem Eng J 2015;262:146–55. https://doi.org/10.1016/j.cej.2014.09.090.
[73] Nichols F, Lu JE, Mercado R, Dudschus R, Bridges F, Chen S. Platinum oxide nanoparticles for electrochemical hydrogen evolution: influence of platinum valence state. Chem - A Eur J 2019:4136–42. https://doi.org/10.1002/chem.201904559.
[74] Wan S, Ou M, Zhong Q, Zhang S, Song F. Construction of Z-scheme photocatalytic systems using ZnIn2S4, CoOx-loaded Bi2MoO6 and reduced graphene oxide electron mediator and its efficient nonsacrificial water splitting under visible light. Chem Eng J 2017;325:690–9. https://doi.org/10.1016/j.cej.2017.05.047.
[75] Chia X, Adriano A, Lazar P, Sofer Z, Luxa J, Pumera M. Layered platinum dichalcogenides (PtS2, PtSe2, and PtTe2) electrocatalysis: monotonic dependence on the chalcogen size. Adv Funct Mater 2016;26:4306–18. https://doi.org/10.1002/adfm.201505402.
[76] Iwashina K, Iwase A, Ng YH, Amal R, Kudo A. Z-schematic water splitting into H2 and O2 using metal sulfide as a hydrogen-evolving photocatalyst and reduced graphene oxide as a solid-state electron mediator. J Am Chem Soc 2015;137:604–7. https://doi.org/10.1021/ja511615s.
[77] Qu A, Xie H, Xu X, Zhang Y, Wen S, Cui Y. High quantum yield graphene quantum dots decorated TiO 2 nanotubes for enhancing photocatalytic activity. Appl Surf Sci 2016;375:230–41. https://doi.org/10.1016/j.apsusc.2016.03.077.
[78] Wang D, Guo L, Zhen Y, Yue L, Xue G, Fu F. AgBr quantum dots decorated mesoporous Bi2WO6 architectures with enhanced photocatalytic activities for methylene blue. J Mater Chem A 2014;2:11716–27. https://doi.org/10.1039/c4ta01444h.